Journal of Materials Chemistry C

PAPER

View Article Online
View Journal | View Issue

Cite this: J. Mater. Chem. C, 2019, 7, 6622

A versatile star-shaped organic semiconductor based on benzodithiophene and diketopyrrolopyrrole†

Qiao He,[a] Munazza Shahid,[a] Julianna Panidi,[b] Adam V. Marsh,[a] Wentao Huang,[b] Matyas Daboczi,[b] Ji-Seon Kim,[b] Zhuping Fei,[c] Thomas D. Anthopoulos[d] and Martin Heeney*[a]

Received 15th February 2019,
Accepted 1st April 2019

DOI: 10.1039/c9tc00905a

rsc.li/materials-c

We report the synthesis of a new star-shaped π-conjugated oligomer, BDT(DPP)$_4$, containing a benzodithiophene core and four diketopyrrolopyrrole arms. The thermal, electrochemical and optical properties are characterized and the results complemented by computational studies. The utility of the molecule is demonstrated in both solar cell and field-effect transistor devices. In the former, BDT(DPP)$_4$ displays low efficiency when used as an acceptor in blends with poly(3-hexylthiophene) but exhibits promising performance as a donor, in blends with either a fullerene or a non-fullerene acceptor. In field-effect transistors BDT(DPP)$_4$ exhibits typical p-type transistor behavior, which is in accordance with its better donor performance in solar cell devices.

1. Introduction

The development of monodisperse π-conjugated oligomers has been an area of significant interest over recent years.[1–5] Such materials can exhibit promising performance in a range of optoelectronic devices, as well as serving as useful models for the behavior of their polymeric analogues. In addition as discrete, well-defined molecules they can typically be prepared in high purity with excellent synthetic reproducibility. Many fascinating linear (one dimensional) oligomers have been reported, but by combining three or more identical conjugated 'arms' onto a central core, rotationally symmetric molecules can also be prepared with higher dimensionality.[6,7] Such materials, often described as star-shaped, can exhibit markedly different properties to those of the conjugated arms alone, with the higher dimensionality resulting in significant changes to molecular assembly and intermolecular interactions.[8] In addition the close proximity of the core and conjugated arms can result in enhanced intramolecular interactions.

Given the fascinating properties that such star-shaped molecules can exhibit, it is unsurprisingly that they have been explored for utilization as an active component in a range of devices such as organic light emitting diodes, field-effect transistors (OFETs) and organic solar cells (OSCs). In the area of OSCs, star-shaped materials have been utilized both as the donor or the acceptor component of the blend. The utilization of star-shaped materials with a twisted 3D geometry has been effective as a method to reduce intermolecular interactions and suppress the formation of large domains within the blend.[9–12] Such large domains are detrimental to performance, since they reduce interfacial area and exciton harvesting.[13–15] It should be noted that although the introduction of intramolecular twisting facilitates smaller domain sizes, it may have detrimental effects on intermolecular π–π stacking and thus charge transport ability of the acceptors in the blends. For example Yan *et al.* reported a series of perylene diimide (PDI) tetramers and demonstrated that decreasing intramolecular twisting could lead to higher electron mobilities, fill factors (FF) and device performance, which is a critical concern for star-shaped molecules.[15,16]

Given the importance of intramolecular twisting on charge carrier mobility and device performance, we were interested to investigate the use of benzo[1,2-*b*:4,5-*b*′]dithiophene (BDT) as the central core of a star-shaped molecule. BDT possesses a large and rigid conjugated structure, which could potentially benefit charge transport due to enhanced delocalization and coplanar π–π stacking. Furthermore conjugated 'arms' can be attached to the BDT core *via* both the 2,6-thienyl positions and

[a] Department of Chemistry and Centre for Plastic Electronics, White City Campus, Imperial College London, London W12 0BZ, UK. E-mail: m.heeney@imperial.ac.uk
[b] Department of Physics and Centre for Plastic Electronics, South Kensington Campus, Imperial College London, London SW7 2AZ, UK
[c] Institute of Molecular Plus, Tianjin Key Laboratory of Molecular Optoelectronic Science, Tianjin University, Tianjin 300072, P. R. China
[d] Division of Physical Sciences and Engineering, King Abdullah University of Science and Technology, Thuwal 23955-6900, Saudi Arabia

† Electronic supplementary information (ESI) available. See DOI: 10.1039/c9tc00905a

the 4,8-phenyl positions. These two positions differ in their steric environments, so different degrees of twisting could be expected for substituents in either position, which may offer interesting opportunities to tune performance. Two-dimensional conjugated polymers based on the BDT unit have achieved great success for application as donor materials in OSCs, because of their deep lying highest occupied molecular orbital (HOMO) level and high hole mobility. However, to the best of our knowledge, there have been only two BDT based star-shaped materials reported so far, with no reports of their application as donors in OSCs or as the semiconductor in an OFET device.[11,17]

In terms of conjugated arms, we focused on thiophene flanked diketopyrrolopyrrole (DPP) units. DPP has been extensively utilized in the development of both electron and hole transporting materials, due to its high backbone planarity and strong intermolecular π–π stacking.[18] It also has an intense absorption in the visible range, which is interesting for potential solar cell applications.[19] There have been previous reports of star-shaped materials containing DPP arms, which have been utilized as either the donor or acceptor materials in solar cell blends, with efficiencies around 5%.[9,20–23] Taking these considerations into account, herein we report the synthesis of a new star-shaped molecule based on BDT as a core and DPP as arms, $BDT(DPP)_4$, and explore its potential application in OFET and OSC devices.

2. Experimental section

2.1. Molecular modeling

Computational details were performed as follows: density functional theory calculations were performed using Gaussian G09 rev.d01 and GaussView 5.0.9 visualization software,[24] using the B3LYP functional.[25,26] Geometry optimizations were performed with full relaxation of all atoms in gas phase without solvent effects. Vibration frequency calculation was performed to check that the stable structures had no imaginary frequency.

2.2. Measurements and characterization

GC-MS was carried out on an Agilent GC 7890A and MS 5975C. Matrix-assisted laser desorption/ionization time-of-flight (MALDI-TOF) mass spectrometry was performed on a Bruker ultrafleXtreme MALDI-TOF analyzer. The ^1H and ^{13}C NMR spectra were measured on a Bruker AVANCE 400 MHz spectrometer and the chemical shifts were given in parts per million. Elemental analysis was performed in a Thermo Scientific (Calro Erba) elemental analyzer, configured for the percentage of C, H, and N. Preparative recycling GPC was run at room temperature using chloroform as eluent. The system consisted of a high pressure liquid chromatography apparatus (JAI LaboACE LC-5060 series) equipped with a pump (P-LA60, flow rate 10 ml min^{-1}), a UV detector (UV-VIS4ch LA, λ = 210 nm, 254 nm, 330 nm, 400 nm) and two columns (Jaigel 2HR and 2.5HR, inner diameter 20 mm × length 600 mm each). UV-vis spectra were recorded on a UV-1601 Shimadzu UV-vis spectrometer. Electrochemical measurements were carried out under nitrogen with a deoxygenated solution of tetra-*n*-butylammonium hexafluorophosphate (0.1 M) in CH_3CN using a computer-controlled CHI660C electrochemical workstation, a glassy-carbon working electrode coated with samples, a platinum-wire auxiliary electrode, and Ag/AgCl as a reference electrode. Potentials were referenced to ferrocenium/ferrocene ($FeCp_2^{+/0}$) couple by using ferrocene as an internal standard. Thermogravimetric analysis (TGA) measurements were performed on a Shimadzu thermogravimetric analyzer (model DTG-60) under a nitrogen flow at a heating rate of 10 °C min^{-1}. Differential scanning calorimetry (DSC) measurements were performed using a Mettler differential scanning calorimeter (DSC822e) under nitrogen at a scanning speed of 10 °C min^{-1}. Atomic force microscope (AFM) images were obtained with Agilent 5500 atomic force microscope system operated in the tapping mode. Samples were prepared following the same procedures for fabrication of solar cells. X-ray diffraction (XRD) measurements were performed on drop-cast films using a Panalytical X'Pert MRD diffractometer equipped with a nickel-filtered Cu $K\alpha_1$ beam and X'Celerator detector using a 40 mA current and 40 kV accelerating voltage. Photoluminescence (PL) spectra were carried out for the neat and blend films (spin-coated on a glass substrate) by using a FLS1000 Photoluminescence Spectrometer (Edinburgh Instruments) with an XE2 continuous xenon lamp. Given their film PL intensities, for P3HT:$BDT(DPP)_4$ and its neat films, an excitation wavelength of 520 nm (3 nm excitation bandwidth (EBW) and 2 nm emission bandwidth (EMBW)) were used. For $BDT(DPP)_4$:C8-ITIC and its neat films, an excitation wavelength of 600 nm (3 nm EBW, 1 nm EMBW) were used. For $BDT(DPP)_4$:$PC_{71}BM$ and its neat films, an excitation wavelength of 520 nm (8 nm EBW, 5 nm EMBW) were used.

2.3. OPV fabrication and characterization

Organic photovoltaic devices were fabricated using regioregular P3HT (M_n = 51 kg mol^{-1}, PDI = 1.76, regioregularity (RR) 97%) as the donor, or C8-ITIC and $PC_{71}BM$ as acceptor materials, blended with $BDT(DPP)_4$ respectively. Devices were fabricated onto pre-patterned ITO covered glass substrates with the device architecture ITO/ZnO/Active layer/MoO_3/Ag. After sequential cleaning of the ITO with the detergent (Decon 90), acetone and isopropyl alcohol, a zinc acetate dihydrate precursor solution (219.5 mg in the mixture of 2 ml 2-methoxyethanol and 60 μl monoethanolamine) was spin coated and was annealed at 200 °C for 50 min. P3HT:$BDT(DPP)_4$ blend solutions were dissolved in chlorobenzene, or $BDT(DPP)_4$:C8-ITIC and $BDT(DPP)_4$:$PC_{71}BM$ blend solutions were dissolved in chloroform with a concentration of 20 mg ml^{-1} and were stirred overnight. The blend solutions were preheated and then spin coated onto the ZnO coated ITO substrate and the thicknesses of the active layers were ~80–100 nm. The active layers were used as-spun or annealed at 130 °C for 10 min. To complete the devices, MoO_3 (*ca.* 10 nm) and Ag (*ca.* 80 nm) were evaporated sequentially under high vacuum (*ca.* 10^{-5} Pa) under shadow masks to fabricate devices with an area of 5 mm^2. Current–voltage characteristics were measured with a Keithley 236 source/measure unit under AM 1.5 solar illumination (Oriel 300 W solar simulator) at an intensity of 100 mW cm^{-2}. All electrical measurements of OPVs

were executed in the inert nitrogen purged devices chamber. External quantum efficiency (EQE) was measured by a 100 W tungsten halogen lamp (Bentham IL1 with Bentham 605 stabilized current power supply) coupled to a monochromator with computer-controlled stepper motor (Bentham M300, 300 mm focal length, slit width 3.7 nm, 1800 lines per m grating) The photon flux of light incident on the samples was calibrated using a UV-enhanced silicon photodiode. A 590 nm long-pass glass filter was inserted into the beam at illumination wavelengths longer than 620 nm to remove light from second-order diffraction. Measurement duration for a given wavelength was sufficient to ensure the current had stabilized.

2.4. OFET fabrication and characterization

Top-gate, bottom-contact (TG-BC) organic field effect transistors were fabricated in order to extract the charge carrier mobility of the material. Glass substrates were sonicated in Decon 90 for 10 minutes, followed by sonication in acetone and isopropanol. Source–drain contacts were formed by thermal evaporation of 40 nm Au followed by 10 nm of $FeCl_3$ in high vacuum (10^{-6} mbar). $FeCl_3$ was used to modify the work function of the evaporated Au. Films were deposited from 10 mg ml^{-1} solutions, that were heated and stirred at 50 °C (chloroform) or 100 °C (chlorobenzene) to ensure $BDT(DPP)_4$ was fully dissolved before spin coating. Spin coating was carried out at 2000 rpm for 60 s, followed by thermal annealing at 100 °C for 15 min. The fluoropolymer dielectric, CYTOP, (900 nm) was spin cast onto the organic semiconductor layer and annealed at 100 °C before aluminium gate electrodes were deposited by thermal evaporation. OFETs were fabricated and tested in a nitrogen atmosphere (glovebox). Electrical measurements were carried out using an Agilent B2902A semiconductor parameter analyser. Charge carrier mobility was extracted from the slope of the $I_D^{1/2}$ *vs.* V_G and the value was then applied to the following equations:

$$\text{For the linear mobility}: \mu_l = \frac{L}{WC_iV_D}\left(\frac{\partial I_{D,l}}{\partial V_G}\right)$$

$$\text{For the saturation mobility}: \mu_s = \frac{2L}{WC_i}\left(\frac{\partial \sqrt{I_{D,s}}}{\partial V_G}\right)^2$$

3. Results & discussion

3.1. Synthesis

The BDT core was initially modified to include two thienyl groups in the 4,8-positions. This was then tetra-borylated using an Ir catalyst to afforded 4,8-diyl(bis(thiophene-5,2-diyl))bis(4,4,5,5-tetramethyl-1,3,2-dioxaborolane) ($BDT\text{-}Bpin_4$) following the reported route.[11] $BDT(DPP)_4$ was then prepared by the fourfold Suzuki coupling reaction between ($BDT\text{-}Bpin_4$) and 3-(5-bromothiophen-2-yl)-2,5-bis(2-ethylhexyl)-6-(thiophen-2-yl)-2,5-dihydropyrrolo[3,4-*c*]pyrrole-1,4-dione (DPP-Br)[27] using $Pd_2(dba)_3/P(MeOPh)_3$ as the catalyst (Scheme 1). The full synthetic routes to all intermediates are shown in Scheme S1 (ESI†). The crude $BDT(DPP)_4$ product from the cross-coupling was initially purified by column chromatography to remove excess DPP-Br and catalyst residues. Although the resulting product appeared to have good purity by ^1H NMR, further purification by recycling preparative gel permeation chromatography (GPC) removed a small impurity, which was identified by MALDI-TOF MS as the trimer, $BDT(DPP)_3$. The final product $BDT(DPP)_4$ was fully characterized by MALDI-TOF MS, ^1H NMR, ^{13}C NMR, and elemental analysis. $BDT(DPP)_4$ was readily soluble in common organic solvents such as dichloromethane, chloroform and chlorobenzene at room temperature, owing to the eight solubilizing 2-ethylhexyl sidechains.

The thermal properties of $BDT(DPP)_4$ were investigated by thermogravimetric analysis (TGA) and differential scanning calorimetry (DSC). $BDT(DPP)_4$ shows good thermal stability with decomposition temperatures (5% weight loss) of over 400 °C in a nitrogen atmosphere (Fig. 1a). Unlike the thermal behavior of previously reported BDT[11] or DPP[9] based star shaped materials which were amorphous, the DSC of $BDT(DPP)_4$ exhibited a relatively sharp melting exotherm at 265 °C with a corresponding endotherm at 183 °C upon cooling, suggestive of a crystalline material (Fig. 1b and Fig. S1, ESI†). Upon second heating a cold crystallization occurred around 195 °C, followed by an identical melting exotherm at 265 °C. The reproducibility of the peaks upon thermal cycling further attests to the good thermal stability of the material.

3.2. DFT calculation

To investigate the structural and electronic properties of $BDT(DPP)_4$, the ground state geometry and frontier molecular

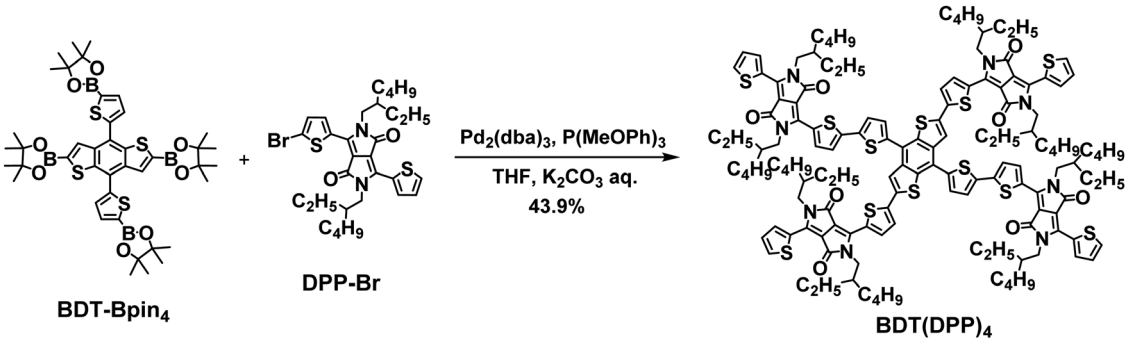

Scheme 1 Synthetic route to compound $BDT(DPP)_4$.

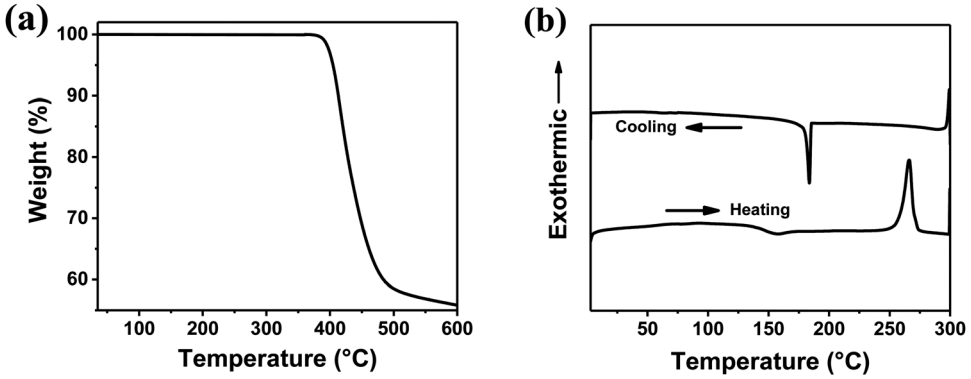

Fig. 1 (a) TGA and (b) DSC curves of BDT(DPP)$_4$ at a heating/cooling speed of 10 °C min^{-1} under N_2.

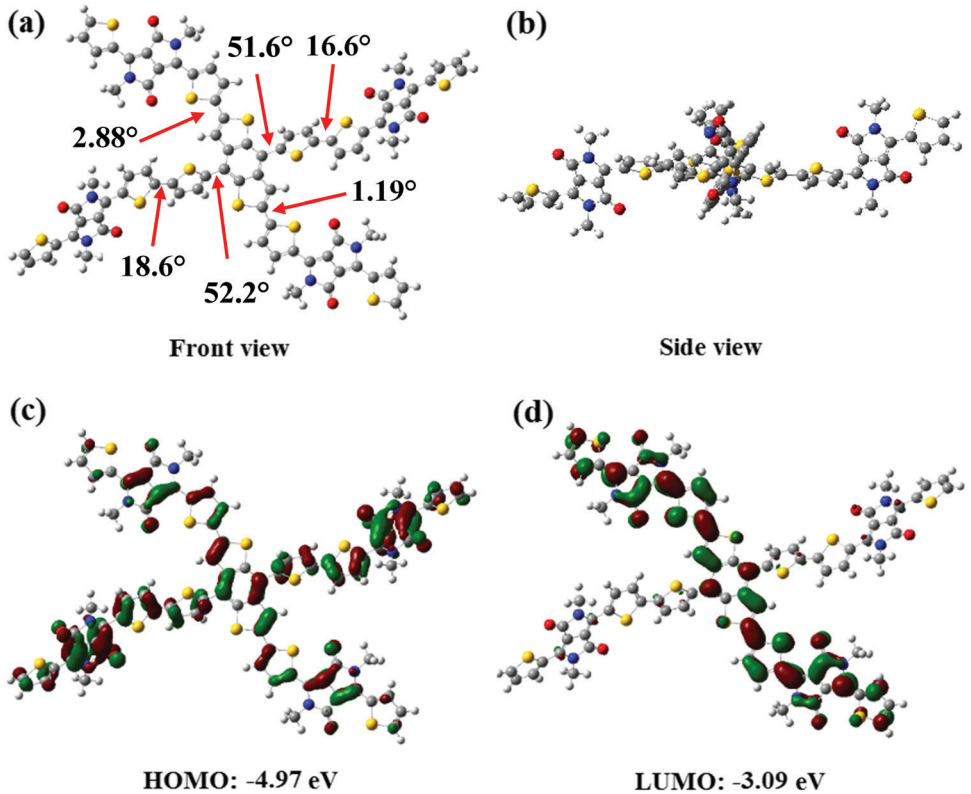

Fig. 2 (a and b) Optimized geometry and (c and d) frontier molecular orbitals of BDT(DPP)$_4$.

orbitals were calculated using density functional theory (DFT) at the B3LYP/6-31G* level (Fig. 2), with all alkyl chains replaced by methyl group for simplicity.[28] The calculations suggest that the planarity of the arms of BDT(DPP)$_4$ is strongly directional, with a near-planar configuration along the molecular axis where the DPP is linked to the 2,6-thienyl positions of BDT, and a more twisted confirmation when linked to the 4,8-phenyl positions of the BDT with a twist angle around 52° (Fig. 2(a and b)). This approximately planar long axis, with a twisted cross-axis is distinctively different to the twisted geometries of reported star-shaped materials. The distributions of the frontier molecular orbital are exhibited in Fig. 2(c and d). The HOMO of BDT(DPP)$_4$ delocalizes throughout the entire molecule despite the large twist in the perpendicular arms, whilst its LUMO is located on the planarised axis. The energy levels of the HOMO and LUMO orbitals are estimated to be −4.97 eV and −3.09 eV respectively, suggesting that the molecule will be predominately a p-type semiconductor.

3.3. Electronic and optical properties

As shown in Fig. 3a, the UV-vis absorption of BDT(DPP)$_4$ solution in chloroform (10^{-6} M) exhibits two peaks, a weak absorption around 400 nm and a strong absorption in 500–650 nm region with a maximum extinction coefficient of 2.78×10^6 M^{-1} cm^{-1} at 590 nm. Upon film formation the λ_{max} of the low energy peak is red-shifted to 622 nm, with the formation of a pronounced longer wavelength shoulder around

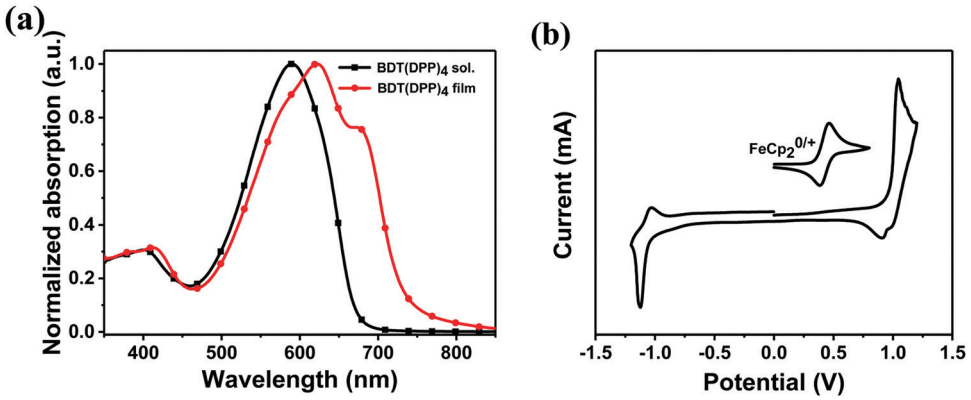

Fig. 3 (a) UV-vis absorption spectra of $BDT(DPP)_4$ in chloroform and as spin-coated film, and (b) cyclic voltammogram of $BDT(DPP)_4$ as drop-cast film in acetonitrile solution containing tetrabutylammonium hexafluorophosphate (0.10 M) with a scanning rate of 0.1 V s^{-1} at room temperature.

690 nm. The red shift is indicative of extended conjugation in the solid state, likely due to enhanced planarity caused by intermolecular interactions of $BDT(DPP)_4$ in the film. The appearance of the longer wavelength shoulder is further indicative of such intermolecular interactions, and has previously been attributed to molecular aggregation.[29] The optical band gap of the $BDT(DPP)_4$ film is 1.69 eV, as estimated from the absorption edge (733 nm).

The electrochemical properties were investigated as a thin film by cyclic voltammetry (Fig. 3b). The LUMO and HOMO energy levels of $BDT(DPP)_4$ were determined to be −3.33 and −5.36 eV respectively, from the onset of the oxidation and reduction peaks relative to reference energy level of ferrocene/ferrocenium (−4.8 eV). The electrochemical band gap is in reasonable agreement with that calculated by DFT, although the absolute experimental values are slightly deeper than those predicted, in agreement with other studies.

3.4. OPV properties

To evaluate the photovoltaic properties of $BDT(DPP)_4$, inverted solar cell devices were fabricated with a configuration of ITO/ZnO/active layer/MoO_3/Ag. As shown in Fig. S2 (ESI†) and Fig. 4b, the film absorption profile and energy levels of $BDT(DPP)_4$ match with those of regioregular poly(3-hexylthiophene) (P3HT), acceptor $PC_{71}BM$, and our previously reported acceptor C8-ITIC[30] (Fig. 4a), with sufficient energetic offsets to potentially act as either the donor or acceptor component. However, utilizing $BDT(DPP)_4$ as an acceptor in blends with P3HT as the donor (blend ratio of 1 : 1) did not make efficient solar cells. Despite exhibiting a decent voltage (0.74 V), a very low PCE of 0.47% was obtained (Table 1 and Fig. 4c), primarily due to the low fill factor (FF) and photocurrent. Attempts to improve the performance by either thermal annealing at 130 °C, solvent annealing or the use of processing additives (Table S1, ESI†) were unsuccessful. Furthermore, the utilization of a different P3HT batch with higher molecule weight (M_n = 68 kDa, PDI = 1.65 and RR = 0.97) did not improve performance.

By applying $BDT(DPP)_4$ as a donor material, more promising PCEs of 3.9% and 2.5% were achieved when blending with C8-ITIC and $PC_{71}BM$ respectively. Both devices gave reasonable photocurrent, 10.1 mA cm^{-2} and 8.54 mA cm^{-2} respectively, but the efficiency was limited by relatively low fill factors, which might result from non-optimal blend morphology. However the use of solvent additive diiodooctane or annealing did not result in improved performance (Table S1, ESI†). The external quantum efficiency (EQE) spectra of the P3HT:$BDT(DPP)_4$, $BDT(DPP)_4$:$PC_{71}BM$ and $BDT(DPP)_4$:C8-ITIC blended films are shown in Fig. 4d. The $BDT(DPP)_4$:C8-ITIC device exhibits higher external quantum efficiencies (EQE = 44%) than the P3HT:$BDT(DPP)_4$ (EQE = 7%) and $BDT(DPP)_4$:$PC_{71}BM$ devices (EQE = 37%) in agreement with the higher device performance. Notably clear photocurrent generation can be observed from absorption of $BDT(DPP)_4$ in the $PC_{71}BM$ blend. The highest performing $BDT(DPP)_4$:C8-ITIC device shows a broader EQE spectra than the P3HT:$BDT(DPP)_4$ and $BDT(DPP)_4$:$PC_{71}BM$ devices, primarily due to the small band gap of the C8-ITIC acceptor. The J_{sc} value calculated from EQE of encapsulated $BDT(DPP)_4$:C8-ITIC device is 9.6 mA cm^{-2}, which matches well with J_{sc} values measured in encapsulated solar cell devices in $<5\%$ deviation.

The surface morphologies of the active blend layers were probed by atomic force microscopy (AFM) and the height and phase images of blended films are shown in Fig. S3 (ESI†). Both the P3HT:$BDT(DPP)_4$ and $BDT(DPP)_4$:$PC_{71}BM$ blends appear relatively smooth with root-mean-square (RMS) roughness of 1.2 nm and 0.8 nm respectively, whilst $BDT(DPP)_4$:C8-ITIC exhibits rougher with a RMS roughness of 3.6 nm. The higher surface roughness probably relates to the high crystallinity of C8-ITIC compared to $PC_{71}BM$ or P3HT. The C8-ITIC blend also shows the presence of what appear to be large crystallites or aggregates on the surface. Such large scale phase segregation would reduce exciton diffusion/separation efficiencies in their blended films and may be a reason for the low fill factor.

The influence of blending on microstructure was further investigated using out-of-plane X-ray diffraction and photoluminescence quenching (PLQ) measurements. Films coated under identical condition to those used for PV devices were used for PLQ measurements, but such film gave very weak diffraction in our XRD set-up, so thicker drop cast films were utilized. Fig. S4 (ESI†) shows the diffraction patterns of P3HT:$BDT(DPP)_4$, $BDT(DPP)_4$:C8-ITIC and $BDT(DPP)_4$:$PC_{71}BM$

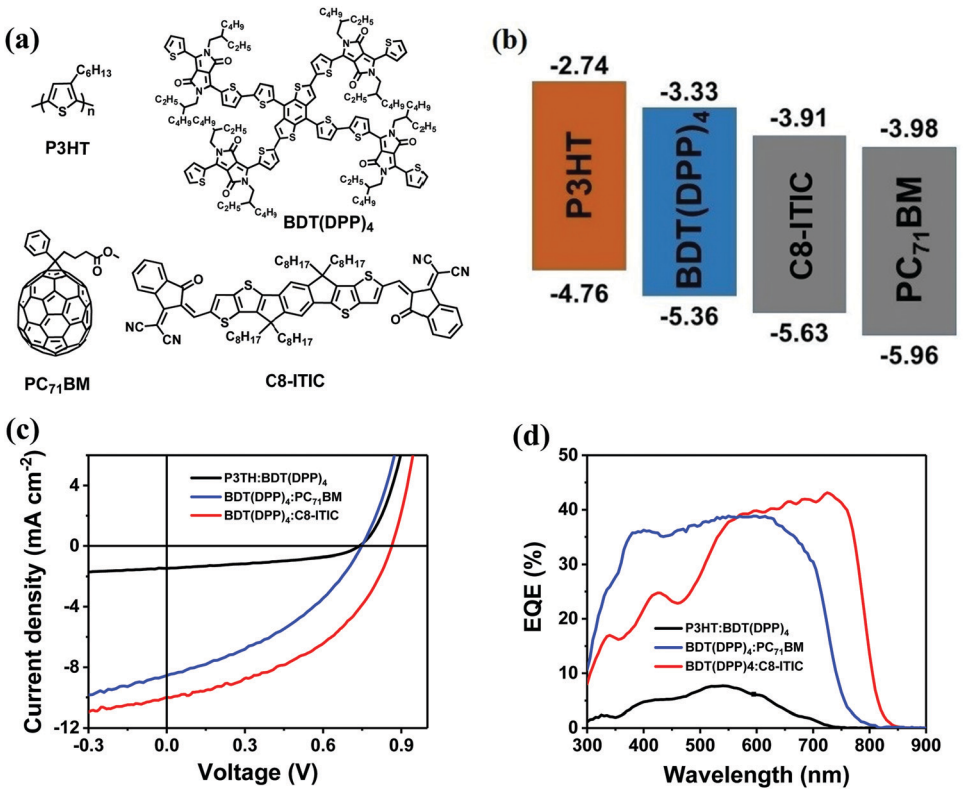

Fig. 4 (a) Chemical structures and (b) energy levels of P3HT, $BDT(DPP)_4$, C8-ITIC and $PC_{71}BM$, (c) *J–V* curves and (d) EQE spectra of OSC devices based on P3HT:$BDT(DPP)_4$, $BDT(DPP)_4$:PC71BM and $BDT(DPP)_4$:C8-ITIC.

Table 1 The *J–V* characteristics of OSC devices based on $BDT(DPP)_4$

Blend	w/w	J_{sc}/mA cm^{-2}	V_{oc}/V	FF	PCE (%)
P3HT:$BDT(DPP)_4$[a,b]	1 : 1	1.5	0.74	0.42	0.47 (0.45)[d]
$BDT(DPP)_4$:$PC_{71}BM$[a]	1 : 2	8.54	0.75	0.39	2.5 (1.9)[d]
$BDT(DPP)_4$:C8-ITIC[c]	1 : 1	10.1	0.86	0.45	3.9 (3.6)[d]

[a] Preheated at 100 °C in chlorobenzene. [b] Annealed at 130 °C for 10 min. [c] Preheated at 50 °C in chloroform. [d] Average PCE values were obtained from over 18 devices.

blend films as well as their respective neat $BDT(DPP)_4$, P3HT, C8-ITIC and $PC_{71}BM$ films. Photoluminescence spectra are shown in Fig. S5 (ESI†). Similar to previous reports,[31] the neat P3HT films exhibited a lamellar diffraction peak at $2\theta = 5.5°$, with weaker second and third order peaks at 11° and 16.5°. $BDT(DPP)_4$ exhibited a weak peak at 5.1°. Upon blending, the P3HT:$BDT(DPP)_4$ film showed a clear diffraction peak corresponding to P3HT, although the second and third order peaks were no longer visible. PLQ measurements using 520 nm excitation demonstrated 90% quenching efficiency upon blending. Whilst indicating that effective photo-induced charge transfer between P3HT and $BDT(DPP)_4$ can occur, the relatively low quenching efficiency suggests that optimum intermixing of the two materials has not occurred, accounting for the low photocurrent and device performance.

For blends of $BDT(DPP)_4$:C8-ITIC, the XRD shows clear peaks corresponding to both the C8-ITIC and the $BDT(DPP)_4$, in accordance with the aggregates observed by AFM. Almost complete photoluminescence quenching (<99%) was also observed upon excitation at 600 nm, indicating effective exciton transport and separation, and likely accounting for the improved performance of this blend. In contrast, the neat $PC_{71}BM$ and blend $BDT(DPP)_4$:$PC_{71}BM$ films did not show any diffraction peaks, suggestive of a relatively amorphous film in agreement with the AFM. The PLQ measurements were complicated due to the weak fluorescence of both $BDT(DPP)_4$ and $PC_{71}BM$, so the bandwidth of excitation and emission slits were adjusted to enlarge the signals. The $BDT(DPP)_4$:$PC_{71}BM$ blend film showed ~88% fluorescence quenching compared to $BDT(DPP)_4$ neat film, again suggestive of non-optimal intermixing.

Overall it is clear that $BDT(DPP)_4$ behaves better as a donor than an acceptor, probably due to the relatively high lying LUMO level. As a donor, its performance compares well to other star-shaped DPP containing materials, which have reported efficiencies up to 4.6% using polymeric acceptors.[19] Furthermore improvements in performance may be possible by tuning of the DPP sidechains or blending with other less crystalline, non-fullerene acceptors.

3.5. OFET properties

The charge transport properties of $BDT(DPP)_4$ were evaluated using organic field effect transistors (OFETs) in a top-gate, bottom contact device configuration (Fig. 5a). Thin films of $BDT(DPP)_4$ were deposited by spin coating from either

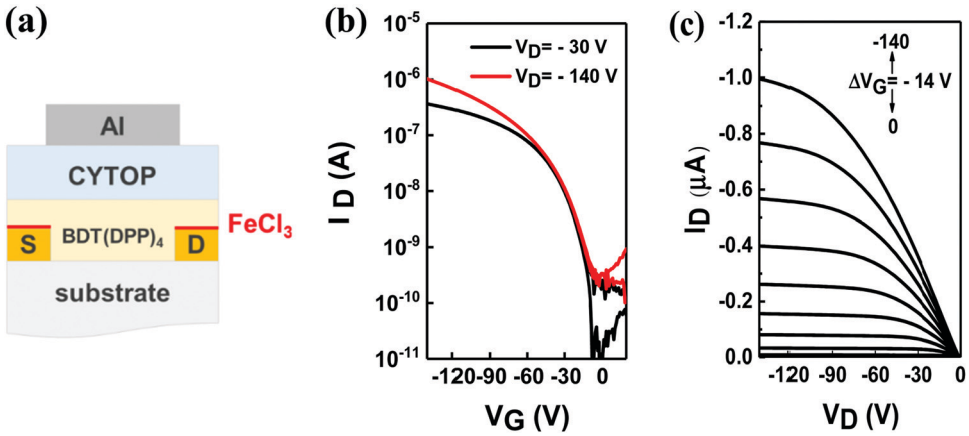

Fig. 5 (a) The top-gate, bottom-contact (TG-BC) transistor architecture employed in this work. (b) Typical transfer characteristics at V_D = −30 V and V_D = −140 V. (c) Output characteristics measured for the same transistor. Transistor channel length (L) and width (W) were 30 μm and 1 mm, respectively.

chloroform or chlorobenzene, followed by annealing at 100 °C. These two solvents were selected as they have different boiling points and it was found that chloroform resulted in slightly improved device performance. Initial devices were fabricated using the as-deposited Au electrodes, in order to probe for possible ambipolar behavior. However, no electron transport could be observed, likely due to the high lying LUMO level. With untreated electrodes there was also clear evidence of contact resistance for hole injection. Therefore a thin layer of amorphous iron(III) chloride was deposited on top of the Au electrodes by thermal evaporation to improve injection, following the reported protocol.[32] Here we note that the semiconductor film was annealed at 100 °C prior to Cytop deposition, which might potentially lead to some diffusion of the $FeCl_3$. However, such uncontrollable dopant diffusion would be expected to result in high off-currents,[33] which were not observed in this case. The typical transfer and output curves for such devices are shown in Fig. 5(b and c) (for films from chloroform) and Fig. S6(a and b) (ESI†) (for films from chlorobenzene). The linear and saturation mobilities are 0.017 and 0.022 $cm^2\ V^{-1}\ s^{-1}$, respectively. This is over one order of magnitude higher than other star shaped materials with DPP arms based on using pyrene or tris(thienyl)benzene cores.[34] The promising performance is likely related to the tendency of molecule to aggregate in the solid phase.

4. Conclusions

In conclusion, we have designed and synthesized a novel star shaped oligomer, $BDT(DPP)_4$, based on BDT as the core with DPP as arms. Small amounts of a trimeric impurity could not be removed by conventional chromatography but were successfully separated by recycling preparative GPC. The optical, thermal and electrochemical properties of $BDT(DPP)_4$ suggest that it undergoes aggregation in the solid state. DFT calculations support this observation, suggesting one molecular axis is nearly coplanar. $BDT(DPP)_4$ is demonstrated to be a versatile semiconducting material, demonstrating promising performance in both organic field effect transistors and organic solar cells. In the latter application it exhibits superior performance when utilized as a donor rather than an acceptor. Device efficiencies up to 3.9% were found when blending with a crystalline non-fullerene acceptor derivative.

Conflicts of interest

There are no conflicts to declare.

Acknowledgements

We thank the China Scholarship Council (CSC) *via* the CSC Imperial Scholarship, the Daphne Jackson Trust (supported by RSC and EPSRC), the Royal Society and the Wolfson Foundation (for Royal Society Wolfson Fellowship) and EPSRC (EP/L016702/1) for financial support.

References

1 J. Roncali, P. Leriche and P. Blanchard, *Adv. Mater.*, 2014, **26**, 3821–3838.
2 S. D. Collins, N. A. Ran, M. C. Heiber and T.-Q. Nguyen, *Adv. Energy Mater.*, 2017, **7**, 1602242.
3 G. Bazan and M. R. Bryce, *J. Mater. Chem. C*, 2016, **4**, 3675–3676.
4 A. Mishra and P. Bäuerle, *Angew. Chem., Int. Ed.*, 2012, **51**, 2020–2067.
5 Y. Lin and X. Zhan, *Acc. Chem. Res.*, 2016, **49**, 175–183.
6 P. J. Skabara, J.-B. Arlin and Y. H. Geerts, *Adv. Mater.*, 2013, **25**, 1948–1954.
7 J. Roncali, P. Leriche and A. Cravino, *Adv. Mater.*, 2007, **19**, 2045–2060.
8 A. L. Kanibolotsky, I. F. Perepichka and P. J. Skabara, *Chem. Soc. Rev.*, 2010, **39**, 2695–2728.

9 S. Li, W. Liu, M. Shi, J. Mai, T.-K. Lau, J. Wan, X. Lu, C.-Z. Li and H. Chen, *Energy Environ. Sci.*, 2016, **9**, 604–610.
10 Z. Luo, T. Liu, W. Cheng, K. Wu, D. Xie, L. Huo, Y. Sun and C. Yang, *J. Mater. Chem. C*, 2018, **6**, 1136–1142.
11 Q. Wu, D. Zhao, A. M. Schneider, W. Chen and L. Yu, *J. Am. Chem. Soc.*, 2016, **138**, 7248–7251.
12 Y. Zhong, M. T. Trinh, R. Chen, G. E. Purdum, P. P. Khlyabich, M. Sezen, S. Oh, H. Zhu, B. Fowler, B. Zhang, W. Wang, C.-Y. Nam, M. Y. Sfeir, C. T. Black, M. L. Steigerwald, Y.-L. Loo, F. Ng, X. Y. Zhu and C. Nuckolls, *Nat. Commun.*, 2015, **6**, 8242.
13 H. Zhong, C.-H. Wu, C.-Z. Li, J. Carpenter, C.-C. Chueh, J.-Y. Chen, H. Ade and A. K. Y. Jen, *Adv. Mater.*, 2016, **28**, 951–958.
14 N. Liang, D. Meng, Z. Ma, B. Kan, X. Meng, Z. Zheng, W. Jiang, Y. Li, X. Wan, J. Hou, W. Ma, Y. Chen and Z. Wang, *Adv. Energy Mater.*, 2017, **7**, 1601664.
15 J. Zhang, Y. Li, J. Huang, H. Hu, G. Zhang, T. Ma, P. C. Y. Chow, H. Ade, D. Pan and H. Yan, *J. Am. Chem. Soc.*, 2017, **139**, 16092–16095.
16 H. Lin, S. Chen, H. Hu, L. Zhang, T. Ma, J. Y. Lai, Z. Li, A. Qin, X. Huang, B. Tang and H. Yan, *Adv. Mater.*, 2016, **28**, 8546–8551.
17 Q. Wu, D. Zhao, J. Yang, V. Sharapov, Z. Cai, L. Li, N. Zhang, A. Neshchadin, W. Chen and L. Yu, *Chem. Mater.*, 2017, **29**, 1127–1133.
18 C. B. Nielsen, M. Turbiez and I. McCulloch, *Adv. Mater.*, 2013, **25**, 1859–1880.
19 A. Tang, C. Zhan, J. Yao and E. Zhou, *Adv. Mater.*, 2017, **29**, 1600013.
20 S.-Y. Liu, J. W. Jung, C.-Z. Li, J. Huang, J. Zhang, H. Chen and A. K. Y. Jen, *J. Mater. Chem. A*, 2015, **3**, 22162–22169.
21 T. Aytun, P. J. Santos, C. J. Bruns, D. Huang, A. R. Koltonow, M. Olvera de la Cruz and S. I. Stupp, *J. Phys. Chem. C*, 2016, **120**, 3602–3611.
22 Y. Zhang, X. Bao, M. Xiao, H. Tan, Q. Tao, Y. Wang, Y. Liu, R. Yang and W. Zhu, *J. Mater. Chem. A*, 2015, **3**, 886–893.
23 X.-F. Wu, W.-F. Fu, Z. Xu, M. Shi, F. Liu, H.-Z. Chen, J.-H. Wan and T. P. Russell, *Adv. Funct. Mater.*, 2015, **25**, 5954–5966.
24 M. J. Frisch, G. W. Trucks, H. B. Schlegel, M. A. R. G. E. Scuseria, J. R. Cheeseman, G. Scalmani, V. Barone, G. A. Petersson, H. Nakatsuji, X. Li, M. Caricato, A. Marenich, J. Bloino, B. G. Janesko, R. Gomperts, B. Mennucci, H. P. Hratchian, J. V. Ortiz, A. F. Izmaylov, J. L. Sonnenberg, D. Williams-Young, F. Ding, F. Lipparini, F. Egidi, J. Goings, B. Peng, A. Petrone, T. Henderson, D. Ranasinghe, V. G. Zakrzewski, J. Gao, N. Rega, G. Zheng, W. Liang, M. Hada, M. Ehara, K. Toyota, R. Fukuda, J. Hasegawa, M. Ishida, T. Nakajima, Y. Honda, O. Kitao, H. Nakai, T. Vreven, K. Throssell, J. A. Montgomery, Jr., J. E. Peralta, F. Ogliaro, M. Bearpark, J. J. Heyd, E. Brothers, K. N. Kudin, V. N. Staroverov, T. Keith, R. Kobayashi, J. Normand, K. Raghavachari, A. Rendell, J. C. Burant, S. S. Iyengar, J. Tomasi, M. Cossi, J. M. Millam, M. Klene, C. Adamo, R. Cammi, J. W. Ochterski, R. L. Martin, K. Morokuma, O. Farkas, J. B. Foresman and D. J. Fox, *Gaussian 09, Revision D.01*, Gaussian, Inc., Wallingford CT, 2016.
25 C. Lee, W. Yang and R. G. Parr, *Phys. Rev. B: Condens. Matter Mater. Phys.*, 1988, **37**, 785–789.
26 A. D. Becke, *J. Chem. Phys.*, 1993, **98**, 5648–5652.
27 L. Huo, J. Hou, H.-Y. Chen, S. Zhang, Y. Jiang, T. L. Chen and Y. Yang, *Macromolecules*, 2009, **42**, 6564–6571.
28 Z. Fei, Y. Han, E. Gann, T. Hodsden, A. S. R. Chesman, C. R. McNeill, T. D. Anthopoulos and M. Heeney, *J. Am. Chem. Soc.*, 2017, **139**, 8552–8561.
29 S. Wood, J. Wade, M. Shahid, E. Collado-Fregoso, D. D. C. Bradley, J. R. Durrant, M. Heeney and J.-S. Kim, *Energy Environ. Sci.*, 2015, **8**, 3222–3232.
30 Z. Fei, F. D. Eisner, X. Jiao, M. Azzouzi, J. A. Röhr, Y. Han, M. Shahid, A. S. R. Chesman, C. D. Easton, C. R. McNeill, T. D. Anthopoulos, J. Nelson and M. Heeney, *Adv. Mater.*, 2018, **30**, 1705209.
31 F. P. V. Koch, M. Heeney and P. Smith, *J. Am. Chem. Soc.*, 2013, **135**, 13699–13709.
32 A. Kumatani, C. Liu, Y. Li, P. Darmawan, K. Takimiya, T. Minari and K. Tsukagoshi, *Sci. Rep.*, 2012, **2**, 393.
33 C. Liu, Y. Xu and Y.-Y. Noh, *Mater. Today*, 2015, **18**, 79–96.
34 S.-Y. Liu, W.-Q. Liu, J.-Q. Xu, C.-C. Fan, W.-F. Fu, J. Ling, J.-Y. Wu, M.-M. Shi, A. K. Y. Jen and H.-Z. Chen, *ACS Appl. Mater. Interfaces*, 2014, **6**, 6765–6775.